# Water column barium sulfate dissolution and shielding by organic matter aggregates: Implications for the pelagic barite proxy

Tricia Light [a,*], Manuel Garcia [a], Jennifer C. Prairie [b], Francisca Martínez-Ruiz [c], Richard Norris [a]

[a] Scripps Institution of Oceanography, University of California, La Jolla, CA 92037, USA
[b] Department of Environmental and Ocean Sciences, University of San Diego, San Diego, CA 92110, USA
[c] Instituto Andaluz de la Ciencias de la Tierra (CSIC-UGR), Avda. de las Palmeras 4, 18100 Armilla, Granada, Spain

## ARTICLE INFO

## ABSTRACT

Pelagic barite ($BaSO_4$) and related proxies are useful tools for reconstructing the marine carbon cycle. The factors controlling pelagic barite dissolution in the ocean water column are poorly understood, which adds uncertainty to Ba-based reconstructions. Here, we conducted static laboratory incubations to test the sensitivity of barium sulfate dissolution rate to a range of commonly occurring seawater pH, salinity, and temperature conditions. We observed relatively rapid dissolution rates ranging from $1.7 \pm 0.4$ to $3.4 \pm 0.8$ pg $BaSO_4$ day$^{-1}$ for these experiments, and we did not observe statistically significant differences in the rate of dissolution with varying pH, salinity, or temperature. The slowest dissolution rate observed in these experiments suggests that an average barium sulfate crystal would survive in the ocean water column just $6.2 \pm 0.3$ days. We estimate that an average isolated pelagic barite crystal would take 67 years to sink down through the water column, so our experiments imply that solitary pelagic barite crystals do not survive this transit. We conducted an additional experiment on a roller table to assess the impact of organic matter aggregates on barium sulfate dissolution. Free barium sulfate crystals incubated on the roller table dissolved even more rapidly than crystals in the static experiment ($19 \pm 7$ pg $BaSO_4$ day$^{-1}$), but barium sulfate crystals incubated with organic matter aggregates showed little sign of dissolution over time. Our findings suggest that organic matter aggregates play a vital role in shielding pelagic barite from dissolution in the water column. This implies that pelagic barite in ocean sediments records the arrival of organic detritus to the seafloor, not just barite crystal formation in sinking organic matter in the upper water column. Additional work is needed to determine which aspects of the marine carbon cycle the pelagic barite proxy captures.

## 1. Introduction

The biological pump, or the export of atmospheric carbon dioxide to the deep ocean and marine sediments in the form of organic carbon, plays an important role in regulating global climate on timescales of tens to thousands of years (DeVries, 2022). Quantifying how the biological pump responds to variable climate, biogeochemical, and ecosystem conditions is vital to accurately predicting how the marine carbon cycle will function in the future (e.g., Fakhraee et al., 2020; Nowicki et al., 2022). Reliable proxies for various components of the marine carbon cycle are required to achieve a nuanced understanding of the past and present biological pump (e.g., Lam et al., 2011; Ma et al., 2015; Winckler et al., 2016). However, proxy interpretation can be complicated by the decoupling of primary productivity in the surface ocean, export

production of organic carbon out of the surface ocean, and organic carbon burial at the seafloor (Lopes et al., 2015).

Pelagic barite is a promising tool for reconstructing various aspects of the marine biological pump (Carter et al., 2020; Horner et al., 2021). Barite is a naturally occurring mineral consisting of barium sulfate ($BaSO_4$), while pelagic or marine barite specifically refers to barite that forms in the ocean water column (e.g., Paytan and Griffith, 2007; Yao et al., 2020). Pelagic barite is ubiquitous in seawater and ocean sediments (Dehairs et al., 1980; Paytan and Griffith, 2007) and occurs as microcrystals that are, on average, approximately 1 μm in length and have a mass of 9–11 pg (Bu et al., 2023; Dehairs et al., 1980; Light and Norris, 2021; Robin et al., 2003). It is thought to precipitate in microenvironments within organic matter aggregates during microbial oxidation, as first proposed by Chow and Goldberg (1960). Given the

---

link between organic matter remineralization and barite precipitation, pelagic barite accumulation rates in ocean sediments have been widely used to reconstruct marine export production (e.g., Costa et al., 2016; Nürnberg et al., 1997; Paytan et al., 1996; Torfstein et al., 2010). However, uncertainties surrounding pelagic barite precipitation and preservation limit it from achieving its full potential as a proxy.

Previous investigations have studied barium sulfate dissolution kinetics and dynamics, particularly in the context of inorganic chemistry and formation of scale in pipelines and well equipment in the oil and gas industries (Higgins et al., 1998; Kamal et al., 2018; Nancollas and Liu, 1975). Observations of barium sulfate dissolution in a closed system reactor demonstrate that barite dissolves with a reaction order of 0.2 with respect to the barium sulfate saturation state ($\Omega_{BaSO_4}$) of the surrounding fluid (Zhen-Wu et al., 2016), as defined by the equation:

$$\Omega_{BaSO_4} = \frac{a_{Ba^{2+}} \times a_{SO_4^{2-}}}{K_{BaSO_4}}$$

where $a$ is the activity of the specified species and $K_{BaSO_4}$ is the equilibrium constant for the dissolution of solid $BaSO_4$ into aqueous $Ba^{2+}$ and $SO_4^{2-}$ ions. The rate-limiting step of barite dissolution is the detachment of a $Ba^{2+}$ ion from the barite surface, which is followed by the relatively fast dissolution of a neighboring $SO_4^{2-}$ ion (Becker et al., 2005). Factors such as temperature, concentrations of background electrolytes, and presence low molecular weight organic compounds and organic chelators can affect the rate of barium sulfate dissolution (e. g., Christy and Putnis, 1993; Dove and Czank, 1995; Dunn et al., 1999; Ouyang et al., 2017; Ouyang et al., 2019; Zhen-Wu et al., 2016). In seawater, pelagic barite solubility has been constrained via laboratory experiments (Burton et al., 1968) and by computation (Church and Wolgemuth, 1972; Hanor, 1969; Rushdi et al., 2000).

Pelagic barite dissolution plays a significant role in the marine barium cycle (e.g., Carter et al., 2020), but the factors controlling it are poorly constrained. Ba and $\delta^{138}$Ba water column profiles in a variety of oceanographic settings are consistent with pelagic barite precipitation in the mesopelagic zone followed by pelagic barite dissolution below 1000 m depth (e.g., Bates et al., 2017; Horner et al., 2015; Horner and Crockford, 2021; Hsieh and Henderson, 2017). The ocean is largely undersaturated with respect to barite, although barite saturation varies geographically and with water depth (Church and Wolgemuth, 1972; Monnin et al., 1999; Rushdi et al., 2000). Seawater is undersaturated with respect to barite in the surface ocean globally and at depth in the Atlantic Ocean, while seawater is at or above saturation below 1000 m in much of the Pacific Ocean (Mete et al., 2023). Meanwhile, observations suggest that pelagic barite burial efficiencies are not predicted by barite saturation indices in the overlying water column (Rahman et al., 2022). Sr/Ba and $\delta^{138}$Ba have been proposed as methods for accounting for variable pelagic barite preservation in the interpretation of sediment barite records (Van Beek et al., 2003; Bridgestock et al., 2018; Bridgestock et al., 2019).

Estimates of water column barite dissolution vary. $^{230}$Th-normalized barium flux measurements suggest average water column barite dissolution rates of 58–69% and 17–46% along transects in the North Atlantic and Eastern Tropical Pacific, respectively (Rahman et al., 2022). Observations in the North Pacific suggest water column dissolution rates of 60 ± 20%, while approximately 10% of water column pelagic barite crystals show dissolution pits and other morphological evidence of dissolution (Light and Norris, 2021). Box models created using sediment trap (Dymond et al., 1992) and pore water (Paytan and Kastner, 1996) data suggest that ~70% of particulate barite flux to the deep ocean dissolves before incorporation into the sediment record. Pelagic barite dissolution rates are high in anoxic ocean basins such as the Black Sea where there is water column sulfate reduction (Falkner et al., 1993), but little is known regarding the controls on barite dissolution rates in oxic waters. Questions remain regarding how variable barite dissolution rates influence sediment barite records (e.g., Schoepfer et al., 2015).

Organic matter aggregates may shield marine barite crystals from dissolution (Carter et al., 2020), but, to our knowledge, the impact of aggregates on barite dissolution has never been directly assessed.

Here, we conducted laboratory experiments to estimate plausible rates of water column pelagic barite dissolution under different chemical and environmental conditions. We compared the dissolution rate of synthetic barium sulfate microcrystals in two sets of experiments. In the organic matter shielding experiment, we assessed differences in the rate of barium sulfate dissolution between crystals encased within organic matter aggregates formed from a diatom culture (the "Aggregate" treatment), free crystals from the water column overlying the aggregates in the aggregate tanks (the "Overlying Water" treatment), and free crystals within a control tank without diatoms added (the "No Aggregate" treatment). In the second set of experiments, we assessed barium sulfate dissolution in free crystals suspended in seawater under a range of salinity, pH, and temperature conditions. We also used Stokes' Law to calculate approximate pelagic barite sinking velocities in the water column to contextualize observed dissolution rates, and we consider the implications for interpretation of marine barite proxies.

## 2. Materials and methods

### 2.1. Barium sulfate crystal synthesis

A protocol was developed to synthesize barium sulfate microcrystals as homogenous in size and morphology as possible. Initially, we tested simpler methods for the formation of barium sulfate. These included addition of $BaCl_2$ to seawater, addition of $BaCl_2$ to artificial seawater in a single step, and addition of $BaCl_2$ to seawater seeded with smaller barium sulfate microcrystals. These methods yielded crystals with a large range of crystal morphologies and sizes within a single batch and were discontinued.

Subsequently, we standardized our methods as follows: for each batch, seawater was collected from the Scripps Institution of Oceanography pier and filtered through a 0.2 um pore size polycarbonate membrane filter (referred to as filtered seawater hereafter). Barium sulfate precipitation was induced by adding 1 mL 10 mM $BaCl_2$ to 49 mL filtered seawater in polypropylene centrifuge tubes. Tubes were shaken and placed in a 4°C refrigerator for 60 min to allow for crystal growth.

Barium sulfate-spiked seawater was then transferred to 1 L polycarbonate bottles, and the bottles were shaken to coat their walls with the seeded barium sulfate solution. These bottles were emptied to remove the initial barium sulfate crystals, which were large and displayed many different morphologies. Seeded bottles were then filled with 32 g NaCl, 4 g $Na_2SO_4$, and 1 L ultrapure Milli-Q water (18.2 MΩ·cm) to produce a basic artificial seawater solution. Bottles were sonicated for 10 min to dissolve the NaCl and suspend barium sulfate nucleation seeds from the bottle walls into the artificial seawater solution. Larger barium sulfate crystals were then formed from the nucleation seeds through the addition of 2 mL 10 mM $BaCl_2$ to each bottle.

Bottles were agitated and placed in a 4°C refrigerator overnight to facilitate ongoing barium sulfate microcrystal growth. The next day, 50 mL of barium sulfate/seawater solution was filtered through a 0.2 um pore size nylon membrane filter for each experiment/treatment. All filters were dried in a 50°C oven and stored until experiment set up.

Crystals were synthesized in one batch for the organic matter shielding experiment and one batch for the pH, salinity, and temperature experiments. We optimized for uniform barium sulfate crystals to facilitate the reliable visual assessment of barium sulfate dissolution over time and to control for morphology or size effects on barite dissolution. Crystals made for the organic matter shielding experiment were larger than those for the pH, salinity, and temperature experiments, but, in both cases, crystals were fairly homogeneous in size and morphology within a synthesis batch (Figs. 1 and 2).
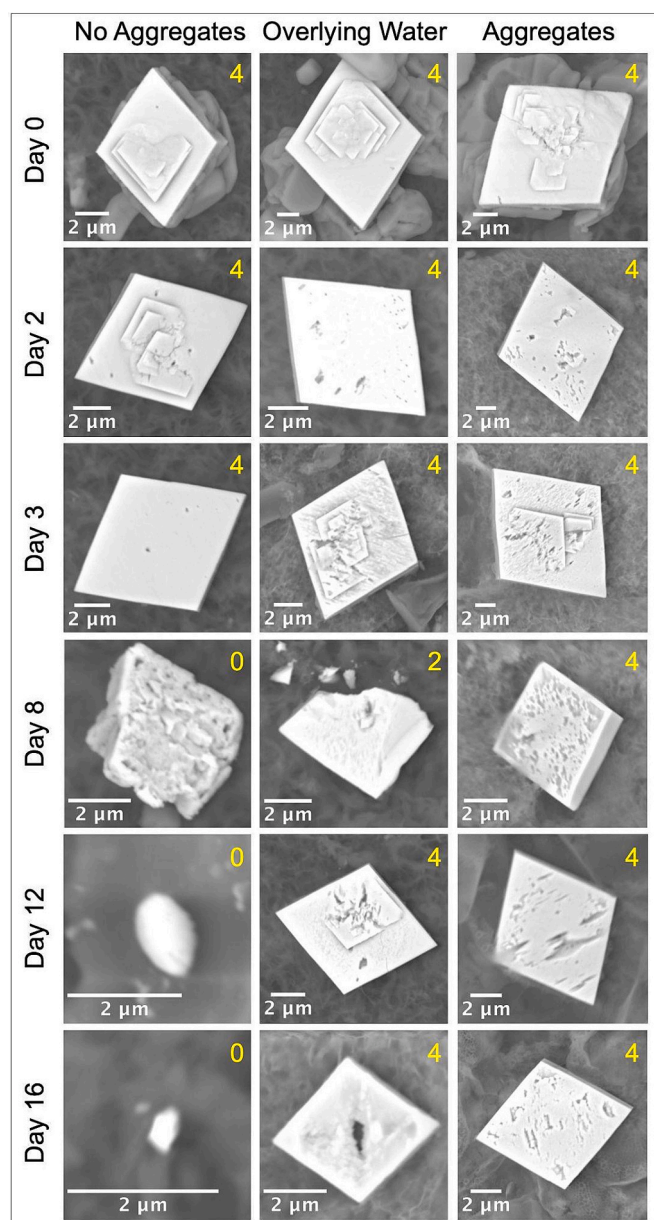
**Fig. 1.** SEM images of representative barium sulfate microcrystals over time from No Aggregate, Overlying Water, and Aggregate treatments of the organic matter shielding experiment. Yellow numbers indicate the number of clearly visible, well-defined crystal faces assigned to each particle. (For interpretation of the references to colour in this figure legend, the reader is referred to the web version of this article.)

### 2.2. Barium sulfate dissolutions rates with organic matter shielding experiment

Non-axenic phytoplankton cultures of the diatom *Thalassiosira weissflogii* were cultured to produce organic matter aggregates in 2 L flasks with f/2 media under a 12:12 h LED light/dark cycle. On day 10, the cell concentration in each culture was measured using a particle counter (Multisizer 3, Beckman Coulter Counter). Cultures were diluted with filtered seawater to a concentration of 20,000 cells mL$^{-1}$ and added to 5 custom-made 2.2 L cylindrical acrylic tanks. Six filters carrying synthesized barium sulfate crystals were each submerged in 50 mL filtered seawater and sonicated for 10 min to suspend the barium sulfate crystals. Filters were removed, and a barium sulfate suspension was added to each of the 5 cylindrical tanks prepared for aggregate

formation and to an additional identical control tank containing only filtered seawater. The control tank was shaken and immediately sampled as described below for an initial time point. All 6 tanks were placed on a roller table and allowed to rotate at a speed of 3.3 rpm, allowing for the formation of aggregates by the diatom cultures. The roller table incubation was conducted at room temperature (20–22°C) and in the dark to prevent any further phytoplankton growth. This method has been widely used in previous studies to form aggregates from phytoplankton in the laboratory (e.g., Prairie et al., 2019).

Subsequent sampling was conducted 2, 3, 8, 12, and 16 days after aggregate formation began (i.e., after tanks were placed on the roller table). For the control tank, 10 mL was sampled via syringe and filtered through a 25 mm diameter 0.2 um pore size nylon membrane filter; this sample became the No Aggregate treatment filter. The filter was then rinsed with 10 mL Milli-Q water to prevent crystallization of salt. Filtered seawater was added to the tank to replace the sampled volume.

For the tanks with aggregates, 1 randomly selected tank was destructively sampled on each sampling day. The tank was removed from the roller table. Organic aggregates were allowed to settle to the bottom of the tank for 2 min, after which 10 mL overlying water was immediately sampled as described above for the control tank to form the Overlying Water treatment filter.

Organic matter aggregates that had settled to the bottom of the tank were photographed on a mm-square grid sealed on the bottom of the roller tank (Fig. A1). Aggregates were then individually removed from the tank using a volumetric pipette with a cut-off tip. The total volume of aggregates from that tank was approximated, and aggregates were filtered through a single 47 mm diameter 0.2 μm pore size polycarbonate membrane filter. The filter made from the aggregates became the Aggregate treatment filter of each experimental tank. The filter was rinsed with 20 mL Milli-Q water to prevent crystallization of salt. All filters were dried and stored until later analysis.

### 2.3. Barium sulfate dissolution rates with varying pH, salinity, and temperature experiments

In addition to the organic matter shielding experiment, we also studied the effects of pH, salinity, and temperature on barite dissolution. Filtered seawater was modified as necessary to achieve 10 experimental treatments (Table 1). pH was adjusted through additions of 0.1 M HCl and 0.1 M NaOH. Salinity was modified by dilution with Milli-Q water or concentration by evaporation over a hotplate. Salinity treatments were then pH adjusted as necessary to replicate unmodified seawater pH. We measured pH and salinity using a multiparameter meter (ProQuatro, YSI). Concentrations of major cations and anions in each experimental treatment were estimated by assuming linear dilution/concentration based on salinity using average seawater values from Emerson and Hedges (2008) (Table A1). Barium concentrations were estimated from linear dilution/concentration from previously published coastal San Diego seawater barium measurements (Esser and Volpe, 2002) (Table A1). These seawater chemistry estimates were used to calculate barite saturation indices for each treatment on The Geochemist's Workbench software (Version 17.0.1; Bethke et al., 2022) using the default thermo.tdat database compiled by Lawrence Livermore National Laboratory (Delany and Lundeen, 1991).

1 L modified seawater from each treatment was added to a 1 L polycarbonate bottle for the incubation. A 50 mL aliquot from each treatment was added to a centrifuge tube with a filter carrying the previously synthesized barium sulfate crystals. Tubes were sonicated for 10 min to resuspend the barium sulfate crystals, and the filters were removed. The contents of each tube were returned to the corresponding seawater treatment bottle, and bottles were agitated. The room temperature treatment was incubated in the dark at room temperature (20–22°C), and all other bottles were incubated in a dark 4°C refrigerator for the remainder of the experiment.

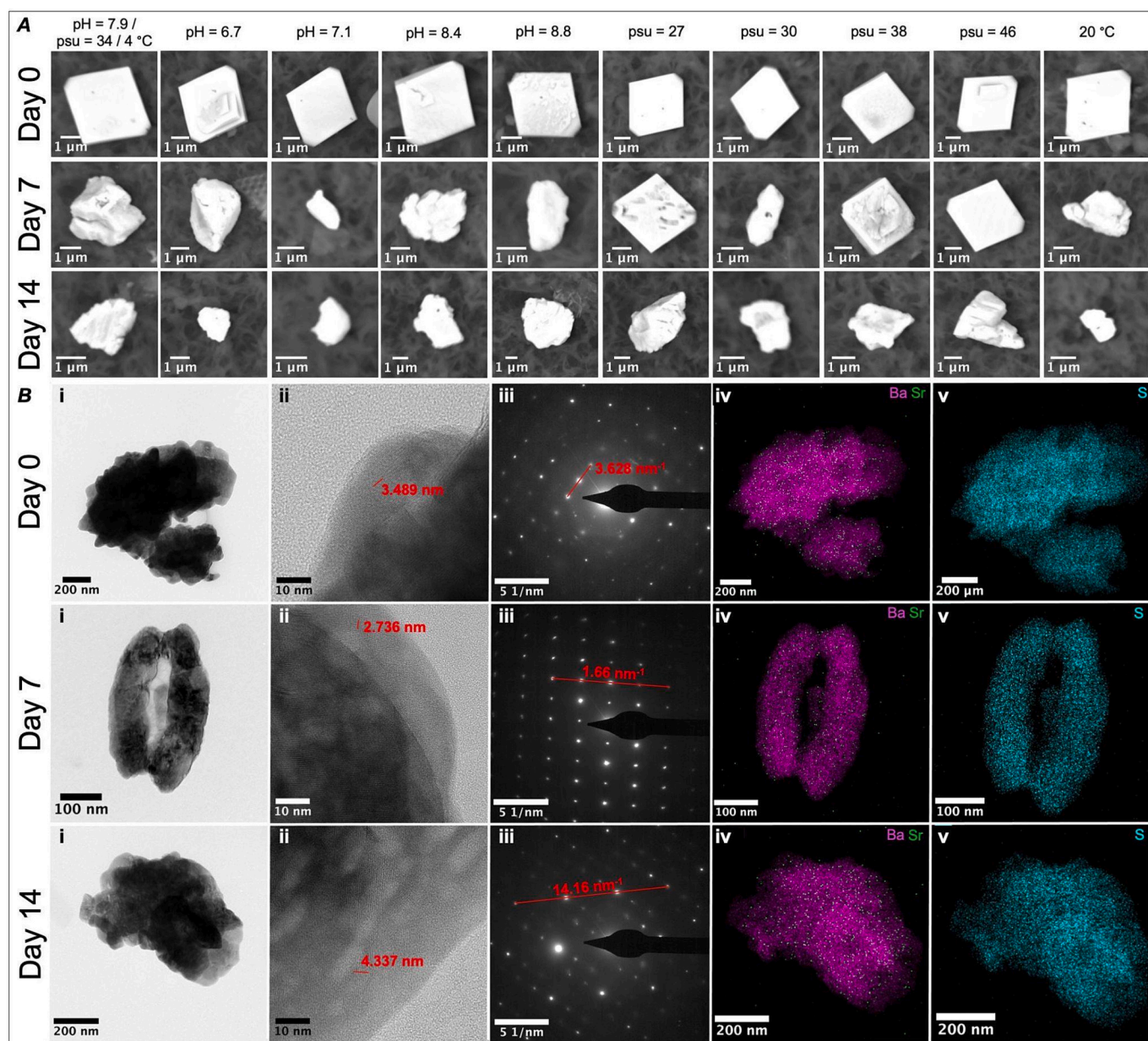Sampling was conducted immediately following experiment set-up

Fig. 2. A) SEM images of representative barium sulfate microcrystals from pH, salinity, and temperature experiments on Day 0, Day 7, and Day 14. B) TEM results for select crystals from Day 0 (pH = 7.9/psu = 34/4°C treatment), Day 7 (psu = 26.7 treatment), and Day 14 (pH = 7.9/psu = 34/4°C treatment). i) HRTEM images. ii) Lattice fringe images, with ten unit cell annotations such that measurements in nm correspond to d-spacings in Å. iii) SAED patterns with characteristic d-space measurements. iv. Ba and Sr and v. S elemental composition maps.

**Table 1**

pH, salinity, temperature, and estimated barium sulfate saturation state for barium sulfate dissolution rate experimental treatments. pH = 7.9/psu = 34/4°C and 20°C treatments used unmodified filtered seawater, and pH and/or salinity were adjusted for all other treatments.

| Treatment | pH | Salinity | Temperature (°C) | $\Omega_{BaSO_4}$ |
|---|---|---|---|---|
| pH = 7.9/psu = 34/4°C | 7.87 | 33.78 | 4 | 0.44 |
| pH = 6.7 | 6.65 | 33.17 | 4 | 0.44 |
| pH = 7.1 | 7.07 | 33.46 | 4 | 0.44 |
| pH = 8.4 | 8.42 | 33.57 | 4 | 0.44 |
| pH = 8.8 | 8.81 | 33.45 | 4 | 0.44 |
| psu = 27 | 7.90 | 26.67 | 4 | 0.34 |
| psu = 30 | 7.97 | 30.04 | 4 | 0.39 |
| psu = 38 | 7.95 | 38.18 | 4 | 0.50 |
| psu = 46 | 7.96 | 45.97 | 4 | 0.62 |
| 20°C | 7.92 | 33.80 | 20–22 | 0.19 |

and after 7, 14, 21, 28, and 35 days. Bottles were shaken to completely mix them. Then, 50 mL was removed from each bottle and filtered through a 25 mm diameter 0.2 um pore size nylon membrane filter. All filters were dried and stored until later analysis.

### 2.4. SEM analysis

Barium sulfate crystal quantity, size, and morphology across treatments and over time were assessed via Scanning Electron Microscopy equipped with Energy-dispersive X-ray Spectroscopy (SEM-EDS). Approximately 1 cm$^2$ of each filter was mounted on an aluminum stub with carbon tape for analysis. Analyses were conducted using a Phenom Desktop SEM with an accelerating voltage of 15 kV, vacuum of 1 Pa, and working distance of 9–10 mm (Scripps Institution of Oceanography).

For the organic matter shielding experiment, 5 randomly selected fields were quantitatively analyzed for each filter. Fields were

0.82–0.91 mm$^2$ for No Aggregates and Overlying Water treatments. Fields were 0.21–0.44 mm$^2$ for the Aggregate treatment due to the much higher density of barium sulfate crystals on these filters. A backscatter electron detector was used to systematically identify all potential barium sulfate crystals within each field by their high atomic number. Identification was confirmed by EDS, and all barium sulfate crystals were imaged. For the pH, temperature, and salinity experiments, potential barium sulfate crystals were identified, their identity was confirmed, and crystals were imaged. The process was repeated until either 15–20 crystals were imaged (28 out of 36 filters) or all visible barium sulfate crystals on the stub were imaged (8 out of 36 filters).

Barium sulfate crystal morphology was assessed via visual image analysis. For the organic matter shielding experiment, images were visually assessed to assign each crystal with its number of clear, well-defined crystal edge faces (Fig. 2). Since crystal surface topography was not always visible, the upward-facing crystal face oriented toward the viewer was not included in these assessments. For both experiments, crystal size was quantitatively determined using the Fiji distribution of ImageJ (Schindelin et al., 2012, 2015). Scaling parameters were extracted from the metadata of each image. Barium sulfate crystals were distinguished from the filter background using the Trainable Weka Segmentation plugin (Arganda-Carreras et al., 2017). Fiji's Analyze Particles plugin was then used to calculate the area, Feret diameter, and best fit ellipse major and minor axis lengths for each crystal. For the organic matter shielding experiment, barium sulfate quantity in each field, defined as total area hereafter, was determined by adding together the areas of every crystal observed in each field. Total area for each field was corrected for the corresponding sample volume according to the equation

$$T = \frac{S \times A_T}{A_F \times V}$$

where T is the total area for a field, S is the sum of individual barium sulfate crystal areas in that field, $A_T$ is the area of the filter, $A_F$ is the area of the field, and V is the volume of seawater filtered through the corresponding filter.

To estimate the mass of barium sulfate crystals imaged, we assumed that barium sulfate crystals with 2 or more well-defined crystal faces had the idealized barite habit of Goldschmidt (1913) barite no. 325, which is most consistent with the rhomboidal two-dimensional barium sulfate images acquired via SEM. We assume that these crystals were imaged from their (0,0,1) face, so crystal thickness in the direction not visible on the SEM was equivalent to the width of the (2,1,0) face. The volume of the crystal, V, can then be estimated by

$$V = A \times c \times L$$

where A is the crystal area visible from the SEM image, c is 0.283, a constant derived from the relative dimensions of crystal thickness: length (crystal axes c: a) of idealized barite no. 325 (Goldschmidt, 1913), and L is the length of the crystal as determined by the Feret diameter. For barium sulfate crystals with 1 or 0 well-defined crystal faces, we assumed that three-dimensional shape could be approximated as an ellipsoid of rotation around the major axis of the best-fit ellipse of each crystal's two-dimensional outline. Crystal volume, V, can then be estimated by

$$V = \frac{4}{3} \times \pi \times \frac{y}{2} \times \left(\frac{x}{2}\right)^{2.}$$

where y and x are the length and width of the best-fit ellipse, respectively. We then used the density of barium sulfate, 4.48 g cm$^{-3}$, to calculate the mass of each barium sulfate crystal based on their estimated volume. The average area per barium sulfate crystal is shown in the Supplementary Material (Figs. A2 and A3).

### 2.5. HRTEM analysis

A subsample of pH, salinity, and temperature experiment filters were analyzed via high resolution transmission electron microscopy (HRTEM) to assess the crystallinity of barium sulfate crystals over time. The following filters were analyzed: pH = 7.9/psu = 34/4°C (Days 0, 7, and 14), pH = 6.7 (Day 7), and psu = 26.7 (Day 7). One quarter of each filter was suspended in ethanol and ground with an agate mortar. Particulate matter suspended in this ethanol was then deposited on carbon-film-coated copper grids. Barium sulfate crystals on these grids were imaged using a FEI TITAN G2 60–300 microscope with a high brightness electron gun (X-FEG) operated at 300 kV and equipped with a Cs image corrector CEOS (Center for Scientific Instrumentation, University of Granada). Elemental composition maps were acquired using a SUPER-X silicon-drift windowless EDX detector. Selected area electron diffraction (SAED) patterns were also collected on barium sulfate crystals. Two to four crystals were imaged for each filter. HRTEM sample preparation preferentially selects for smaller crystals, so only SEM images were used to evaluate barium sulfate crystal size and morphology.

### 2.6. Statistical analyses

ANCOVAs were conducted to compare the rate of change of experimental parameters between treatments over time. For the organic matter shielding experiment, ANCOVAs were conducted on cube root transformed total area, natural log transformed mass per crystal, and average number of crystal faces per field over time. Since no organic matter aggregates were present on Day 0, crystal total area, mass per crystal, and crystal face measurements from the No Aggregate treatment were used as the initial time point for Aggregate and Overlying Water treatments as well. For pH, salinity, and temperature experiments, ANCOVAs were conducted to compare the rate of change in estimated mass per crystal over time between treatments. Mass per crystal was cube root transformed, square root transformed, and natural log transformed for pH, salinity, and temperature data, respectively. Across all experiments, linear regressions were conducted for each treatment when rates of change appeared to significantly differ between treatments. Linear regressions were conducted across treatments when no significant interaction effect was observed. For total area, all treatments were cube root transformed. For mass per crystal, No Aggregate and Aggregate treatments were square root transformed, and the overlying water treatment was natural log transformed. For number of crystal faces, all treatments were square root transformed. For all data, assumptions of normality and homoscedasticity were assessed via Q-Q and residual-fitted plots. All statistical analysis was performed in R Version 3.6.3 (R Core Team, 2020), and the ggplot package was used for data visualization (Wickham, 2016).

### 2.7. Barite sinking velocity calculations

An idealized spherical pelagic barite crystal was used to calculate an approximate barite sinking velocity through the water column. Sinking velocity was calculated according to Stokes' law

$$S_V = \frac{2}{9} \times g \times r^2 \times \frac{\rho_{barite} - \rho_{seawater}}{\eta_{seawater}}$$

where $S_V$ is sinking velocity, g is Earth's gravitational acceleration (9.81 m s$^{-2}$), r is the radius of the sphere, $\rho_{barite}$ is the density of barite (4480 kg m$^{-3}$), $\rho_{seawater}$ is the density of seawater, and $\eta_{seawater}$ is the dynamic viscosity of seawater. The radius of the sphere was calculated from a crystal area of $0.90 \pm 0.03$ µm$^2$, the average area of intermediate depth pelagic barite crystals in the North Pacific (Light and Norris, 2021). $\rho_{seawater}$ and $\eta_{seawater}$ values for seawater with salinity of 35 g kg$^{-1}$ at a temperature of 10°C were used (Nayar et al., 2016; Sharqawy et al., 2010). The Reynolds number ($R_e$) of this idealized barite crystal was

calculated using

$$R_e = \frac{2 \times \rho_{seawater} \times S_v \times r}{\eta_{seawater}}$$

to determine if Stokes' Law applied to the sinking particle. $R_e$ was $<0.1$, so Stokes' Law does apply (McNown and Malaika, 1950).

## 3. Results

### 3.1. Barium sulfate dissolutions rates with organic matter shielding

Immediately following experiment set-up, most ($> 90\%$) barium sulfate crystals formed regularly-shaped rhombuses with 4 clear, well-defined crystal edge faces (Fig. 3). Most initial crystals displayed stair-stepped surface topography (Fig. 3). Organic matter aggregates were visible in all phytoplankton tanks by day 2 of the incubation and became smaller and better-defined over time (Fig. A1). Barium sulfate crystals from the Aggregate treatment showed little change in morphology over the course of the incubation. The only observed change in crystals removed from the Aggregate treatment was that stair-stepped surface topography was less common and pitted surface topography was more common later in the incubation (Fig. 3). Crystals from the Overlying

Water treatment crystals displayed a mixture of rhomboidal and irregular morphologies by day 3, with some crystals displaying pits and other visual evidence of dissolution (Fig. 3). By day 8, most barium sulfate crystals from the No Aggregate treatment displayed irregular morphologies (Fig. 3).

The rate of change for total crystal area, mass per crystal, and average number of crystal faces over time depended on experimental treatment (ANCOVAs; $F_{2,74} = 5.266$, $p = 0.007$; $F_{2,584} = 15.569$, $p < 0.001$; and $F_{2,80} = 5.918$, $p = 0.004$, respectively). Total crystal area decreased over time for the No Aggregate treatment and did not significantly change over time for the Overlying Water or Aggregate treatments (Table 2). Mass per crystal decreased over time for the No Aggregate treatment, increased over time for the Aggregate treatment, and did not significantly change over time for the Overlying Water treatment (Table 2). The number of crystal faces significantly declined over time for the No Aggregate treatment, but no significant change over time was observed for the other treatments (Table 2).

### 3.2. Barium sulfate dissolution with varying pH, salinity, and temperature

On day 0, most ($> 95\%$) barium sulfate crystals were regularly shaped rhombuses (Fig. 2). On day 7, approximately half of observed crystals were rhomboidal and half displayed irregular morphologies
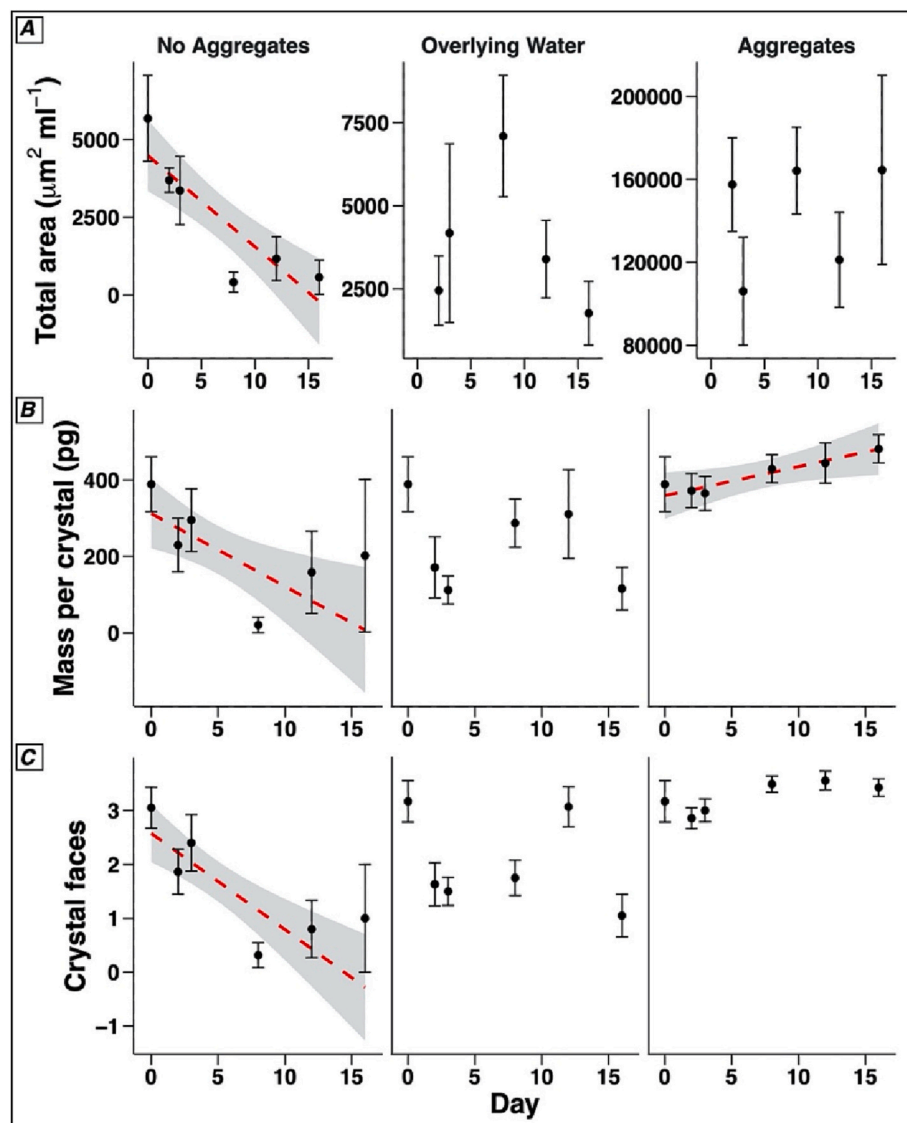


**Fig. 3.** Barium sulfate A) total area per field, B) mass per crystal, and C) average number of well-defined crystal faces per field over time for No Aggregates, Overlying Water, and Aggregate treatments of the organic matter shielding experiment. Red dashed lines show fitted linear regression curves with standard error in gray for all parameters with a statistically significant ($p < 0.05$) change over time (see Table 2 for statistics and regression values). (For interpretation of the references to colour in this figure legend, the reader is referred to the web version of this article.)

**Table 2**

Linear regression values for No Aggregate, Overlying Water, and Aggregate treatments of the organic matter shielding experiment. Regressions were calculated with time in days as the independent variable.

| Regression | F | df | p-value | r² | m | b |
|---|---|---|---|---|---|---|
| Total area (µm² mL⁻¹) | | | | | | |
| No Aggregates | 34.57 | 1, 28 | < 0.001 | 0.55 | −290 ± 60 | 4500 ± 600 |
| Overlying Water | 0.49 | 1, 23 | 0.492 | 0.02 | – | – |
| Aggregates | 0.08 | 1, 23 | 0.774 | 0 | – | – |
| | | | | | | |
| Mass per crystal (pg) | | | | | | |
| No Aggregates | 13.50 | 1, 90 | < 0.001 | 0.13 | −19 ± 7 | 310 ± 50 |
| Overlying Water | 2.74 | 1, 158 | 0.100 | 0.02 | – | – |
| Aggregates | 7.40 | 1, 336 | 0.045 | 0.01 | 8 ± 3 | 360 ± 30 |
| | | | | | | |
| Crystal faces | | | | | | |
| No Aggregates | 13.47 | 1, 24 | 0.001 | 0.36 | −0.15 ± 0.05 | 2.8 ± 0.4 |
| Overlying Water | 0.18 | 1, 28 | 0.679 | 0.01 | – | – |
| Aggregates | 1.83 | 1, 28 | 0.187 | 0.06 | – | – |

(Fig. 2). On day 14, approximately 90% of crystals displayed irregular morphologies, and some crystals displayed etching and dissolution pits (Fig. 2). Beginning on day 21, barium sulfate crystals across treatments displayed globular morphologies and were larger than crystals from day 0 (Fig. A4). These large, globular morphologies suggested that the aggregation of barium sulfate microcrystals had occurred, so samples from day 21 and later were excluded from subsequent analyses. All barium sulfate crystals analyzed via HRTEM displayed well-defined crystallinity (Fig. 2). Lattice-fringe images and SAED patterns yielded d-space measurements consistent with barium sulfate. There was no significant difference in the rate of change in crystal mass over time between treatments for pH, salinity, and temperature variation experiments (ANCOVAs, $F_{1,227} = 2.903$, $p = 0.090$; $F_{1,204} = 0.603$, $p = 0.438$; $F_{1,91} = 3.261$, $p = 0.074$, respectively). Since there was no significant difference in the rate of change between treatments, we conducted a single regression for each treatment to determine the overall rate of change in crystal mass over time. These regressions revealed that crystal mass significantly decreased over time across treatments for all three experiments (Fig. 4 and Table 3).

These results can be used to estimate how long typical pelagic barite crystals survive in the ocean water column. We observed barium sulfate dissolution rates ranging from 19 ± 7 pg day⁻¹ for the No Aggregates treatment of the organic matter shielding experiment (Table 2) to 1.7 ± 0.4 pg day⁻¹ for the salinity variation experiment (Table 3). Thus, we can use the slowest dissolution rate from the salinity variation experiment to estimate an upper threshold for average pelagic barite crystal survival time. The mean mass per crystal of pelagic barite was 10.0 ± 2.4 pg and 10.6 ± 2.2 pg in surface sediments collected from the North Pacific and North Atlantic, respectively (Robin et al., 2003). At a dissolution rate of 1.7 ± 0.4 pg day⁻¹, barite crystals of mean mass would entirely dissolve after 5.9 ± 0.3 and 6.2 ± 0.3 days. Crystals would last only half a day under the faster rate of dissolution suggested by the No Aggregates treatment.

We can compare these estimated survival times to the approximate amount of time it takes a typical pelagic barite crystal to sink down through the water column. The estimated sinking velocity of an average-sized pelagic barite crystal (length 1.08 µm; see Methods for details) is 0.14 m day⁻¹. At this sinking velocity, a barite crystal would sink only 87 ± 4 cm from its point of formation in 6.2 ± 0.3 days, or the estimated average barite survival time calculated above. In contrast, a pelagic
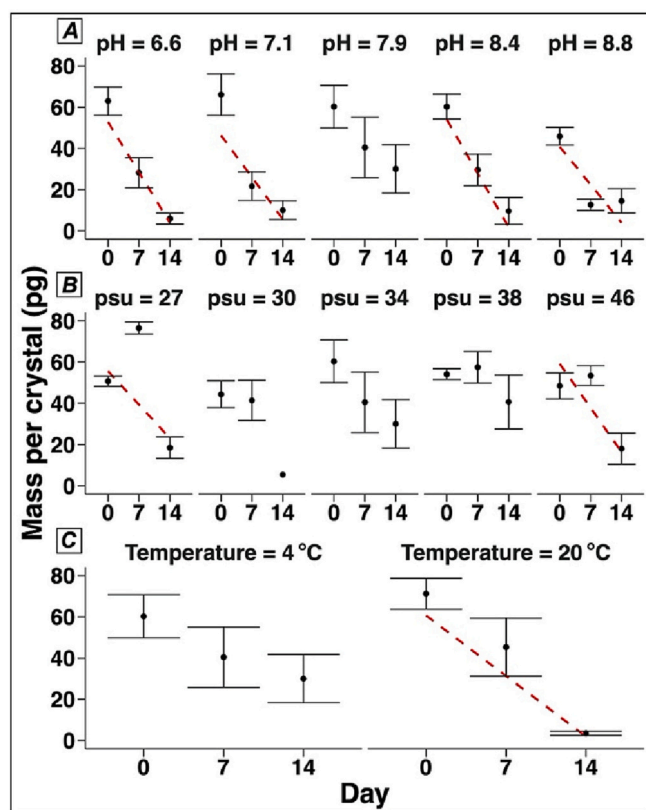


**Fig. 4.** Barium sulfate mass per crystal over time for free crystals in the A) pH, B) salinity, and C) temperature variation experiments. Red dashed lines show fitted linear regression curves for each treatment with a statistically significant ($p < 0.05$) change over time (see Table A2 for regression values). Interaction between treatment and rate of change in crystal mass over time was insignificant for all three experiments, so treatment-specific regressions were calculated for visualization purposes only. Regressions for each experiment are presented in Table 3. (For interpretation of the references to colour in this figure legend, the reader is referred to the web version of this article.)

**Table 3**

Linear regression values for pH, salinity, and temperature experiments. A single regression was conducted using data from all treatments within each experiment. Regressions were calculated with time in days as the independent variable and crystal mass as the dependent variable.

| Regression | F | df | p-value | r² | m (pg) | b (pg) |
|---|---|---|---|---|---|---|
| pH | 139.4 | 1, 229 | < 0.001 | 0.38 | −3.2 ± 0.4 | 56 ± 3 |
| Salinity | 28.9 | 1, 206 | < 0.001 | 0.12 | −1.7 ± 0.4 | 54 ± 4 |
| Temperature | 23.6 | 1, 93 | < 0.001 | 0.20 | −3.4 ± 0.8 | 66 ± 7 |

barite crystal sinking at a velocity of 0.14 m day⁻¹ would take 67 years to sink from a point of formation at 200 m depth to a seafloor depth of 3500 m.

## 4. Discussion

### 4.1. Rapid dissolution of free barium sulfate crystals

Barium sulfate crystal quantity, mass and morphology over time across all experiments suggest that barium sulfate crystals not encased within organic matter aggregates dissolve within days when exposed to surface ocean seawater. We observed statistically significant declines in crystal total area and mass per crystal for all experiments and treatments without organic matter aggregates (Figs. 1–4). Additionally, the enumeration of well-defined faces for each crystal provided a

quantitative measure for the qualitative observation that barium sulfate crystal morphology changed over time (Fig. 3). Since most barium sulfate crystals displayed four well-defined crystal edge faces at the beginning of the incubation, subsequent declines in the number of crystal faces were likely due to dissolution. HRTEM analyses confirm that barium sulfate crystals displayed a high degree of crystallinity throughout the incubation, so the observed changes in morphology were due to crystal dissolution (Fig. 2). A range of crystal sizes and morphologies were observed within each treatment on any given day (Figs. 2 and 3), which suggests that there is natural variability in barium sulfate dissolution. Our analyses of covariance revealed no statistically significant changes in the rate of barium sulfate dissolution with pH, salinity, or temperature over time (Fig. 4).

While barium sulfate dissolution was observed across all treatments without organic matter aggregates, rates of dissolution did vary between experiments. The rate of dissolution in the salinity experiment was slightly slower than that of the pH and temperature experiments (Table 3). This may be a function of sampling variability, particularly since we imaged a relatively small number of crystals for each treatment. The rate of barium sulfate dissolution in the No Aggregate treatment of the organic matter shielding experiment was higher than that of the pH, salinity, or temperature experiments. The organic matter shielding experiment was conducted at room temperature on a roller table, so the No Aggregate treatment crystals likely dissolved more quickly in part because they were exposed to fluid resistance resembling a crystal sinking down through the ocean water column. While we did not observe a statistically significant difference in barium sulfate dissolution rate in our temperature variation experiment, the higher temperature of the organic matter shielding experiment may have also contributed the more rapid dissolution rate in this treatment.

Since we only directly measured changes in barium sulfate crystal area over time, our experiments are limited in their ability to provide detailed insights into the kinetics of barium sulfate dissolution in seawater. However, we can use our estimates of barium sulfate mass loss over time combined with estimated surface area per crystal on Day 0 to determine surface area normalized rate of barium sulfate dissolution (Table A3). The surface area normalized dissolution rates we observed were slightly slower than those reported for similar experiments in Zhen-Wu et al. (2016). For example, we calculated a surface area normalized dissolution rate of $-0.7 \pm 0.3 \times 10^{-8}$ mol m$^{-2}$ s$^{-1}$ for the No Aggregate treatment, while a rate constant from Zhen-Wu et al. (2016) predicts a barium sulfate dissolution rate of $-2.2 \times 10^{-8}$ mol m$^{-2}$ s$^{-1}$ in a 1 mol kg$^{-1}$ NaCl solution with an equivalent $\Omega_{BaSO_4}$ (Table A3). Zhen-Wu et al. (2016) observed modest changes in barium sulfate dissolution rate with pH and larger changes with increased ionic strength and temperature. However, these experiments were conducted using a wider range of pH, ionic strength, and temperature conditions than those found in the natural seawater. Our experiments suggest that barium sulfate dissolution rate varies little within commonly observed ocean pH, salinity, temperature conditions, but a more rigorous investigation into the kinetics of barium sulfate dissolution in seawater would be helpful for further constraining these relationships.

Additionally, we conducted our experiments with synthetic barium sulfate rather than naturally occurring pelagic barite, so our experiments are limited in their ability to fully reproduce pelagic barite dissolution in the water column. In some ways, the use of synthetic barium sulfate crystals likely underestimates pelagic barite dissolution. Synthetic barium sulfate crystals likely lacked structural defects that occur in naturally occurring pelagic barite (Light and Norris, 2021; Sun et al., 2015), so they may have been less susceptible to dissolution. Similarly, our barium sulfate crystals were formed in the absence of Sr$^{2+}$ and other trace elements, but pelagic barite contains 10 mg strontium per g of barite on average (Averyt and Paytan, 2003). Strontium incorporation increases the solubility of pelagic barite relative to pure barium sulfate (Monnin and Cividini, 2006; Rushdi et al., 2000; Widanagamage et al., 2014), so this may lead to an underestimation of pelagic barite

dissolution rates. Pelagic barite is also 5–15 times smaller than the barium sulfate crystals we observed at the beginning of our experiments (Figs. 1 and 2; Bertram and Cowen, 1997; Light and Norris, 2021), so pelagic barite generally has a larger surface area to volume ratio than our synthetic crystals. The larger size of our synthetic crystals compared to marine crystals may have led to slower observed dissolution rates because dissolution is dependent on crystal surface area (e.g., Lüttge, 2005) and increases with decreasing crystal size (Briese et al., 2017). In contrast with these other discrepancies, the morphology of our synthetic barium sulfate crystals may have caused our rates to overestimate pelagic barite dissolution. Pelagic barite is generally ellipsoidal, but our experimental crystals were euhedral (Figs. 1 and 2; Bertram and Cowen, 1997; Light and Norris, 2021). Dissolution is enhanced at crystal edges (Trindade Pedrosa et al., 2019), so pelagic barite may have dissolved more slowly than our synthetic crystals under the same experimental conditions.

Despite these limitations, we can use our observations to estimate plausible pelagic barite dissolution rates in the water column. Our findings suggest that variation in pelagic barite dissolution rates with pH, salinity, and temperature is very small relative to the difference between estimated barite crystal survival and sinking times in the water column. The longest estimated survival time suggested by our experiments for an average pelagic barite crystal ($6.2 \pm 0.3$ days) is much shorter than the estimated time that it would take the average pelagic barite crystal to sink down 3300 m to the seafloor (67 years). The coastal, surface ocean seawater used in our incubations likely had a lower barite saturation state than deep seawater in much of the ocean (Mete et al., 2023). However, most pelagic barite precipitation occurs within the upper 1000 m of the water column, where barite undersaturation is widespread (Carter et al., 2020). Therefore, pelagic barite survival in the upper ocean is vital to barite transport throughout the water column. Our measured barium sulfate dissolution rates across a range of feasible seawater pH, salinity, and temperature conditions suggest that free pelagic barite is unlikely to survive transit through an ocean water column.

The changes in barium sulfate crystal size and morphology observed in the pH, temperature, and salinity experiments between days 14 and 21 suggest barium sulfate microcrystal aggregation began to occur in these treatments. While all treatments were undersaturated with respect to barium sulfate at the beginning of the experiment (Table 1), ongoing barium sulfate dissolution during the experiment released both Ba$^{2+}$ and SO$_4^{2-}$ into the ambient seawater. We did not monitor the concentration of Ba$^{2+}$ and SO$_4^{2-}$ in the ambient seawater over time. However, since we added up to 1 μmol barium sulfate to each treatment at the beginning of the experiment and observed considerable barium sulfate dissolution over time (Fig. 4), it is likely that the ambient seawater was at or near barium sulfate saturation by day 21. Barium sulfate microcrystal aggregation and nonclassical growth is well-documented (e.g., Judat and Kind, 2004; Kügler et al., 2015; Marchisio et al., 2002), so the aggregation of partially dissolved barium sulfate crystals may have been facilitated by these conditions. This transition from barium sulfate dissolution to aggregation highlights a shortcoming in our experimental design, particularly over longer time scales. Future investigations should consider maintaining a constant degree of barium sulfate undersaturation throughout the experiment by tracking Ba$^{2+}$ and SO$_4^{2-}$ concentrations over time and diluting treatments as needed. We would have likely observed even greater rates of barium sulfate dissolution if we had taken such measures.

### 4.2. Organic matter aggregates shield barium sulfate crystals from dissolution

Barium sulfate crystal quantity, mass, and morphology over time in the organic matter shielding experiment suggest that organic matter aggregates protect barium sulfate from dissolution in seawater undersaturated with respect to seawater. Barium sulfate crystals sampled from

the Overlying Water treatment showed no statistically significant changes in size or morphology over the course of the incubation. The only statistically significant change observed for the Aggregate treatment was a small increase in mass per crystal for the average population of crystals within aggregates (Table 2 and Fig. 3). The only visibly observable change in barium sulfate crystals over time for Aggregate and Overlying Water treatments was a slight change in surface topography (Fig. 1), which suggests that barium sulfate dissolution may occur within organic matter aggregates but over much longer time scales than those studied here.

Organic matter aggregates likely shield barium sulfate from dissolution through physical and chemical mechanisms, both in our experiments and in the ocean water column. Interstitial flow through organic matter aggregates is limited (Ploug et al., 2002; Zetsche et al., 2020), so aggregates form a physical barrier that may protect barite from fluid resistance from the water column. Small-scale chemical gradients can form within sinking aggregates (Alldredge and Silver, 1988; Ploug, 2001), so aggregates may also shield barite from dissolution by limiting diffusion and creating microenvironments with higher barite saturation states than the surrounding water column. Aggregates are held together by extracellular polymeric substances (EPS), which have been shown to bioaccumulate $Ba^{2+}$ (Martinez-Ruiz et al., 2018). It is possible that this bioaccumulation not only facilitates pelagic barite precipitation but also subsequently protects crystals from dissolution.

While sinking velocities were not experimentally tested here, incorporation into aggregates likely also promotes pelagic barite preservation by increasing the sinking velocities of crystals. Settling velocities for organic matter aggregates range from 10 to 1000 m day$^{-1}$ depending on the characteristics of the aggregate (e.g., Iversen and Ploug, 2010; Laurenceau-Cornec et al., 2020). These velocities are 70–7000 times faster than the estimated sinking velocity for an average-sized free barite crystal. Similarly, the incorporation of high-density pelagic barite crystals into organic matter aggregates may increase their sinking velocity. Experiments show that ballast materials such as opal and atmospheric dust increase the sinking velocity of aggregates, so pelagic barite may also be an effective aggregate ballast (Iversen and Ploug, 2010; van der Jagt et al., 2018).

The similarities between barium sulfate crystals in the Aggregate and Overlying Water treatments (Figs. 1 and 3) suggest that even very small organic matter aggregates or transparent exopolymeric particle (TEP) films coating barium sulfate crystals are sufficient to shield crystals from dissolution. While our Overlying Water treatment samples contained few, if any, visible organic matter aggregates, they undoubtedly contained subvisible aggregates and TEP. Shielding by these smaller particles likely explains the limited dissolution of Overlying Water treatment crystals (Figs. 1 and 3), and these results suggest that subvisible marine particles also play a role in pelagic barite dynamics.

In our incubation and in natural seawater, marine organic matter aggregates grow over time through coagulation, or the collisions of smaller particles due to processes such as fluid shear, Brownian motion, and particle settling (Alldredge and Jackson, 1995). These processes, combined with the stickiness of EPS, likely explain how barium sulfate was efficiently incorporated into aggregates, since total barium sulfate area was much higher in Aggregate treatment filters than the other treatments (Fig. 3). Ongoing coagulation may also explain the increase in mass per crystal over time for the average population of crystals within aggregates (Fig. 3). Earlier in the incubation, aggregates likely incorporated some smaller crystals which had undergone partial dissolution in the surrounding seawater before colliding with an aggregate. By the end of the incubation, many of these surrounding crystals had likely dissolved completely, so the average population of Aggregate treatment barite included fewer of these smaller crystals.

### 4.3. Implications for the barite proxy

Together, these findings suggest that organic matter aggregates are

vital to the survival of pelagic barite crystals as they sink through seawater undersaturated with respect to barite (Fig. 5). When barite crystals precipitate within aggregates but those aggregates then disintegrate, the barite crystals will likely dissolve well before they sink to the seafloor. The fraction of aggregates that survive transit through the water column is poorly constrained. However, aggregates are well-known to represent hotspots for bacterial activity (e.g., Ziervogel et al., 2010) and a common food source for zooplankton (e.g., Cawley et al., 2021). Due to these pressures, much of the organic matter within aggregates is remineralized as these aggregates sink through the water column (DeVries and Weber, 2017; Sanders et al., 2014). Therefore, most pelagic barite crystals will dissolve before they reach the seafloor, as is consistent with prior mass balance estimates (Paytan and Kastner, 1996).

Under this hypothetical scenario, the free barite crystals that are observed in the water column (e.g., Light and Norris, 2021; Xiao et al., 2022) have likely been recently released by organic matter aggregates that have been degraded or fragmented. A small fraction of these free crystals may be incorporated into other aggregates, given their stickiness and rapid sinking velocity compared to crystals. However, since aggregate formation occurs primarily in surface waters (Simon et al., 2002), most barite particles released into seawater undersaturated with respect to barite likely dissolve. This suggests that microbial activity and associated EPS production play an essential role in both pelagic barite formation (Gonzalez-Muñoz et al., 2012; Martinez-Ruiz et al., 2019; Torres-Crespo et al., 2015) and pelagic barite preservation. Our findings also show that seawater properties such as pH, salinity, and temperature have a much smaller effect on barite dissolution than a crystal's association with an organic matter aggregate. This increases our confidence in pelagic barite as a reliable, widely applicable carbon cycle proxy.

Nonetheless, the impact of spatial variability in water column barite dissolution on sediment barite accumulation rates and proxy interpretations should be explored. Recent work shows that micro-scale barite dissolution and precipitation fractionate Ba isotopes (Middleton et al., 2023), so the shielding of barite crystals by organic matter aggregates may also have implications for barite as a record of Ba isotopes. The factors influencing pelagic barite dissolution at the sediment-water interface also warrant further study. Finally, the role of subvisible TEP particles in shielding barite crystals from dissolution bears further analysis since our experiments suggest that crystals experimentally exposed to diatom cultures but not associated with large aggregates were also protected from dissolution.

An important implication of our findings is that the sediment pelagic barite proxy is likely to most closely track not organic matter remineralization or export out of the surface ocean but rather the flux of organic matter aggregates to the sediment-water interface. Our laboratory experiments are inherently limited in their ability to recreate marine conditions, so this hypothesis must be tested in the field. Previous proxy calibrations have compared the accumulation rate of pelagic barite in marine sediments to surface ocean productivity or export production (Hayes et al., 2021; Eagle et al., 2003; Paytan et al., 1996). If pelagic barite crystals require shielding by organic matter aggregates to survive transport through the water column, we would expect pelagic barite accumulation rates to correlate more closely with proxies for the arrival of organic matter to the seafloor. These proxies include the abundance of benthic foraminifera, organic carbon, organic phosphorous, calcium carbonate, and opal in core top sediments (e.g., Brummer and Van Eijden, 1992; Bareille et al., 1991; Loubere, 1991; Pedersen and Calvert, 1990; Schenau and De Lange, 2001). However, these proxies have their own limitations in terms of preservation (e.g., Calvert and Pedersen, 2007; Ragueneau et al., 2000; Schoepfer et al., 2015), and pelagic barite formation is linked to microbial activity and EPS formation, which is not always well-correlated with foraminifera production (e.g., Martinez-Ruiz et al., 2020).

Some previous investigations have presented collocated core top Ba or barite data along with one or more of the other proxies listed above,
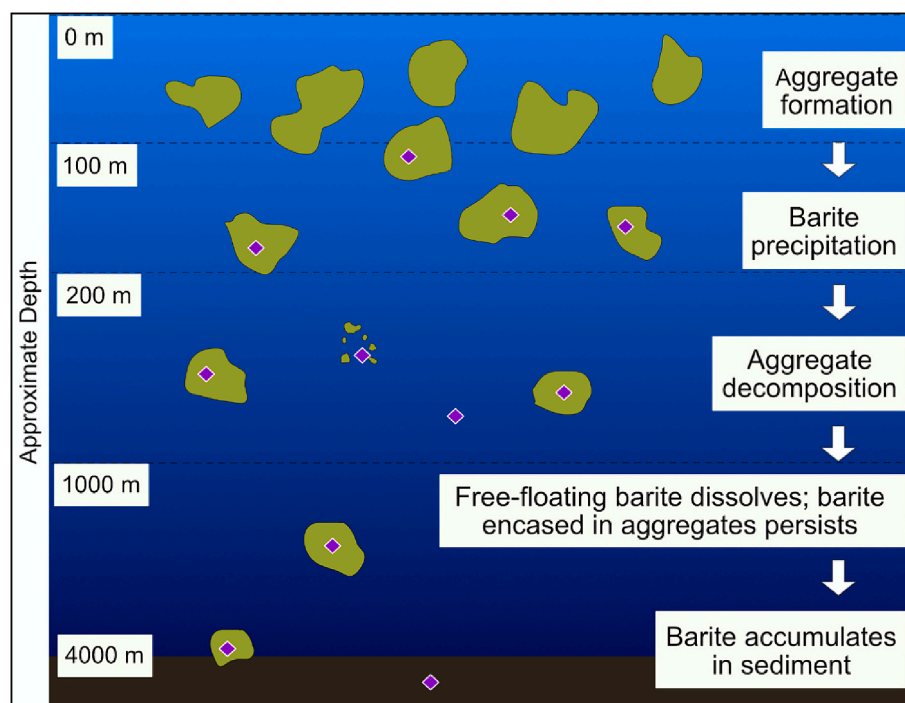
**Fig. 5.** Schematic illustrating the proposed role of organic matter aggregates (depicted in green) in protecting pelagic barite crystals (depicted as purple diamonds) from dissolution in the water column. Schematic is not to scale, and water depths are approximate as each of the processes listed occur over a wide range of depths. (For interpretation of the references to colour in this figure legend, the reader is referred to the web version of this article.)

allowing us to test our hypothesis (Hayes et al., 2021; Schoepfer et al., 2015; Serno et al., 2014; Shen et al., 2023). Reanalysis of these datasets yields mixed results, with excess barium sometimes showing stronger positive correlations with organic matter accumulation proxies than surface-based measures of productivity (Table A4). A larger scale investigation specifically targeted at comparing core top pelagic barite accumulation with multiple other carbon cycle proxies from a variety of locations is likely needed to reliably assess which water column processes are recorded by sediment barite abundance.

If our hypothesis regarding the water column dissolution of free barite crystals is correct, it may undermine recent interpretations of some paleoceongraphic records. Griffith et al. (2021) and Diester-Haass and Faul (2019) found that pelagic barite accumulation rates were decoupled from benthic foraminiferal accumulation rates during Eocene hyperthermals in the South Atlantic and in the Paleogene Southern Ocean, respectively. These studies attributed this decoupling to pelagic barite recording export production out of the mesopelagic and benthic foraminifera recording the supply of organic matter and therefore food to the seafloor (Diester-Haass and Faul, 2019; Griffith et al., 2021). They suggest that these parameters diverge when there is a change in an ecosystem's transfer efficiency, or the fraction of organic matter that is exported out of the euphotic zone that reaches the deep ocean. This explanation relies on pelagic barite crystals surviving transit through the water column even when not shielded by organic matter aggregates. This might have been facilitated by a higher seawater barite saturation state during the Paleogene. However, Sr/Ba measurements suggest that barite undersaturation during the Paleocene-Eocene Thermal Maximum was comparable to that of the modern ocean (Paytan et al., 2007). Alternatively, benthic foraminifera may have only been able to consume a subset of the organic matter aggregates that shielded pelagic barite from dissolution, or ecosystem pressures independent from organic matter supply may have influenced benthic foraminifera populations. Palaeoceanographic studies from different locations and time periods generally show agreement between pelagic barite accumulation and benthic foraminifera (e.g., Gorbarenko et al., 2007; Moore Jr et al., 2014; Reolid and Martínez-Ruiz, 2012), so additional work is needed to

determine how barite sediment records shed light on transfer efficiency and other vital aspects of the marine carbon cycle.

## 5. Conclusions

Here, we conducted laboratory experiments to assess the dissolution rate of synthetic barium sulfate in seawater under different conditions. We found that pH, salinity, and temperature did not significantly affect the observed rate of barium sulfate dissolution. Our findings suggest that pelagic barite dissolution in undersaturated seawater is far too rapid to allow for free barite crystals to survive transit through the water column. In contrast, barium sulfate crystals encased within organic matter aggregates showed little evidence of dissolution over time. This suggests that organic matter aggregates are critical to shielding pelagic barite crystals from dissolution. Therefore, the sediment pelagic barite proxy likely tracks the flux of organic matter aggregates to the seafloor. These findings call attention to the need for additional field-based studies to determine which water column processes are captured by sediment barite abundance. This has potentially important implications for the interpretation of sediment pelagic barite records to gain new insights into the marine carbon cycle.

## Declaration of Competing Interest

None.

## Data availability

Datasets related to this article can be found hosted on the Open Science Framework at doi:10.17605/OSF.IO/JFQDA.

*Declaration of competing interest*

The authors declare that they have no known competing financial interests or personal relationships that could have appeared to influence the work reported in this paper.

## Appendix A. Supplementary data

Supplementary data to this article can be found online at https://doi. org/10.1016/j.chemgeo.2023.121637.

## References

Alldredge, A.L., Jackson, G.A., 1995. Preface: aggregation in marine system. Deep Sea Res. Part II: Top. Stud. Oceanogr. 42, 1–7. https://doi.org/10.1016/0967-0645(95) 90003-9.

Alldredge, A.L., Silver, M.W., 1988. Characteristics, dynamics and significance of marine snow. Prog. Oceanogr. 20, 41–82. https://doi.org/10.1016/0079-6611(88)90053-5.

Arganda-Carreras, I., Kaynig, V., Rueden, C., Eliceiri, K.W., Schindelin, J., Cardona, A., Sebastian Seung, H., 2017. Trainable Weka segmentation: a machine learning tool for microscopy pixel classification. Bioinformatics 33, 2424–2426. https://doi.org/ 10.1093/bioinformatics/btx180.

Averyt, K.B., Paytan, A., 2003. Empirical partition coefficients for Sr and Ca in marine barite: implications for reconstructing seawater Sr and Ca concentrations. Geochem. Geophys. Geosyst. 4, 1043. https://doi.org/10.1029/2002GC000426.

Bareille, G., Labracherie, M., Labeyrie, L., Pichon, J.J., Turon, J.L., 1991. Biogenic silica accumulation rate during the Holocene in the southeastern Indian Ocean. Mar. Chem. 35, 537–551. https://doi.org/10.1016/S0304-4203(09)90041-X.

Bates, S.L., Hendry, K.R., Pryer, H.V., Kinsley, C.W., Pyle, K.M., Woodward, E.M.S., Horner, T.J., 2017. Barium isotopes reveal role of ocean circulation on barium cycling in the Atlantic. Geochim. Cosmochim. Acta 204, 286–299. https://doi.org/ 10.1016/j.gca.2017.01.043.

Becker, U., Biswas, S., Kendall, T., Risthaus, P., Putnis, C.V., Pina, C.M., 2005. Interactions between mineral surfaces and dissolved species: from monovalent ions to complex organic molecules. Am. J. Sci. 305, 791–825. https://doi.org/10.2475/ ajs.305.6-8.791.

Bridgestock, L., Hsieh, Y.T., Porcelli, D., Homoky, W.B., Bryan, A., Henderson, G.M., 2018. Controls on the barium isotope compositions of marine sediments. Earth Planet. Sci. Lett. 481, 101–110. https://doi.org/10.1016/j.epsl.2017.10.019.

Bertram, M.A., Cowen, J.P., 1997. Morphological and compositional evidence for biotic precipitation of marine barite. J. Mar. Res. 55 (3), 577–593. https://doi.org/ 10.1357/0022240973224292.

Bethke, M.C., Farrell, B., Yeakel, S., 2022. GWB Essentials Guide. Aqueous Solutions, LLC.

Bridgestock, L., Hsieh, Y.T., Porcelli, D., Henderson, G.M., 2019. Increased export production during recovery from the Paleocene–Eocene thermal maximum constrained by sedimentary Ba isotopes. Earth Planet. Sci. Lett. 510, 53–63. https:// doi.org/10.1016/j.epsl.2018.12.036.

Briese, L., Arvidson, R.S., Luttge, A., 2017. The effect of crystal size variation on the rate of dissolution–A kinetic Monte Carlo study. Geochim. Cosmochim. Acta 212, 167–175. https://doi.org/10.1016/j.gca.2017.06.010.

Brummer, G.J.A., Van Eijden, A.J.M., 1992. "Blue-ocean" paleoproductivity estimates from pelagic carbonate mass accumulation rates. Mar. Micropaleontol. 19, 99–117. https://doi.org/10.1016/0377-8398(92)90023-D.

Bu, X., Liu, M., Ding, Y., Yang, Y., Huang, M., Sun, X., Fan, D., Yang, Z., 2023. The origin and preservation of suspended barites near the 90° E ridge in the northeastern Indian Ocean. J. Ocean Univ. China 22, 88–98. https://doi.org/10.1007/s11802-023-5257-6.

Burton, J.D., Marshall, N.J., Phillips, A.J., 1968. Solubility of barium sulphate in sea water. Nature 217, 834–835. https://doi.org/10.1038/217834a0.

Calvert, S.E., Pedersen, T.F., 2007. Chapter 14 Elemental proxies for palaeoclimatic and palaeoceanographic variability in marine sediments: interpretation and application. In: Hillaire-Marcel, C., De Vernal, A. (Eds.), Proxies in Late Cenozoic Paleoceanography. Elsevier, Amsterdam, pp. 567–644. https://doi.org/10.1016/ S1572-5480(07)01019-6.

Carter, S.C., Paytan, A., Griffith, E.M., 2020. Toward an improved understanding of the marine barium cycle and the application of marine barite as a paleoproductivity proxy. Minerals 10, 421. https://doi.org/10.3390/min10050421.

Cawley, G.F., Décima, M., Mast, A., Prairie, J.C., 2021. The effect of phytoplankton properties on the ingestion of marine snow by *Calanus pacificus*. J. Plankton Res. 43, 957–973. https://doi.org/10.1093/plankt/fbab074.

Chow, T.J., Goldberg, E.D., 1960. On the marine geochemistry of barium. Geochim. Cosmochim. Acta 20, 192–198. https://doi.org/10.1016/0016-7037(60)90073-9.

Christy, A.G., Putnis, A., 1993. The kinetics of barite dissolution and precipitation in water and sodium chloride brines at 44–85 C. Geochim. Cosmochim. Acta 57, 2161–2168. https://doi.org/10.1016/0016-7037(93)90557-D.

Church, T.M., Wolgemuth, K., 1972. Marine barite saturation. Earth Planet. Sci. Lett. 15, 35–44. https://doi.org/10.1016/0012-821X(72)90026-X.

Costa, K.M., McManus, J.F., Anderson, R.F., Ren, H., Sigman, D.M., Winckler, G., Fleisher, M.Q., Marcantonio, F., Ravelo, A.C., 2016. No iron fertilization in the equatorial Pacific Ocean during the last ice age. Nature 529, 519–522. https://doi. org/10.1038/nature16453.

Dehairs, F., Chesselet, R., Jedwab, J., 1980. Discrete suspended particles of barite and the barium cycle in the open ocean. Earth Planet. Sci. Lett. 49, 528–550. https://doi. org/10.1016/0012-821X(80)90094-1.

Delany, J.M., Lundeen, S.R., 1991. The LLNL Thermochemical Data Base–Revised Data and File Format for the EQ3/6 Package. No. UCID-21658. Lawrence Livermore National Lab (LLNL), Livermore.

DeVries, T., 2022. The ocean carbon cycle. Annu. Rev. Environ. Resour. 47, 317–341. https://doi.org/10.1146/annurev-environ-120920-111307.

DeVries, T., Weber, T., 2017. The export and fate of organic matter in the ocean: new constraints from combining satellite and oceanographic tracer observations. Glob. Biogeochem. Cycles 31, 535–555. https://doi.org/10.1002/2016GB005551.

Diester-Haass, L., Faul, K., 2019. Paleoproductivity reconstructions for the Paleogene Southern Ocean: A direct comparison of geochemical and micropaleontological proxies. Paleoceanogr. Paleoclimatol. 34 (1), 79–97. https://doi.org/10.1029/ 2018PA003384.

Dove, P.M., Czank, C.A., 1995. Crystal chemical controls on the dissolution kinetics of the isostructural sulfates: celestite, anglesite, and barite. Geochim. Cosmochim. Acta 59, 1907–1915. https://doi.org/10.1016/0016-7037(95)00116-6.

Dunn, K., Daniel, E., Shuler, P.J., Chen, H.J., Tang, Y., Yen, T.F., 1999. Mechanisms of surface precipitation and dissolution of barite: a morphology approach. J. Colloid Interface Sci. 214, 427–437. https://doi.org/10.1006/jcis.1999.6224.

Dymond, J., Suess, E., Lyle, M., 1992. Barium in deep-sea sediment: a geochemical proxy for paleoproductivity. Paleoceanography 7, 163–181. https://doi.org/10.1029/ 92PA00181.

Eagle, M., Paytan, A., Arrigo, K.R., van Dijken, G., Murray, R.W., 2003. A comparison between excess barium and barite as indicators of carbon export. Paleoceanography 18. https://doi.org/10.1029/2002PA000793.

Emerson, S., Hedges, J., 2008. Chemical Oceanography and the Marine Carbon Cycle. Cambridge University Press, Cambridge. https://doi.org/10.1017/ CBO9780511793202.

Esser, B.K., Volpe, A.M., 2002. At-sea high-resolution chemical mapping: extreme barium depletion in North Pacific surface water. Mar. Chem. 79, 67–79. https://doi.org/ 10.1016/S0304-4203(02)00037-3.

Fakhraee, M., Planavsky, N.J., Reinhard, C.T., 2020. The role of environmental factors in the long-term evolution of the marine biological pump. Nat. Geosci. 13, 812–816. https://doi.org/10.1038/s41561-020-00660-6.

Falkner, K.K., Klinkhammer, G.P., Bowers, T.S., Todd, J.F., Lewis, B.L., Landing, W.M., Edmond, J.M., 1993. The behavior of barium in anoxic marine waters. Geochim. Cosmochim. Acta 57, 537–554. https://doi.org/10.1016/0016-7037(93)90366-5.

Goldschmidt, V.M., 1913. Atlas der Krystallformen. Carl Winters Universitätsbuchhandlung, Heidelberg.

Gonzalez-Muñoz, M.T., Martinez-Ruiz, F., Morcillo, F., Martin-Ramos, J.D., Paytan, A., 2012. Precipitation of barite by marine bacteria: a possible mechanism for marine barite formation. Geology 40, 675–678. https://doi.org/10.1130/G33006.1.

Gorbarenko, S.A., Goldberg, E.L.V., Kashgarian, M., Velivetskaya, T.Y.A., Zakharkov, S. P., Pechnikov, V.S., Bosin, A.A.E., Psheneva, O.Y.E., Ivanova, E.D., 2007. Millennium scale environment changes of the Okhotsk Sea during last 80 kyr and their phase relationship with global climate changes. J. Oceanogr. 63, 609–623. https://doi.org/ 10.1007/s10872-007-0054-1.

Griffith, E.M., Thomas, E., Lewis, A.R., Penman, D.E., Westerhold, T., Winguth, A.M., 2021. Bentho-pelagic decoupling: The marine biological carbon pump during Eocene hyperthermals. Paleoceanogr. Paleoclimatol. 36 (3), e2020PA004053 https://doi. org/10.1029/2020PA004053.

Hanor, J.S., 1969. Barite saturation in sea water. Geochim. Cosmochim. Acta 33, 894–898. https://doi.org/10.1016/0016-7037(69)90036-2.

Hayes, C.T., Costa, K.M., Anderson, R.F., Calvo, E., Chase, Z., Demina, L.L., Dutay, J.-C., German, C.R., Heimbürger-Boavida, L.E., Jaccard, S.L., Jacobel, A., Kohfeld, K.E., Kravchishina, M.D., Lippold, J., Mekik, F., Missiaen, L., Pavia, F.J., Paytan, A., Pedrosa-Pamies, R., Petrova, M.V., Rahman, S., Robinson, L.F., Roy-Barman, M., Sanchez-Vidal, A., Shiller, A., Tagliabue, A., Tessin, A.C., van Hulten, M., Zhang, J., 2021. Global ocean sediment composition and burial flux in the deep sea. Glob. Biogeochem. Cycles 35. https://doi.org/10.1029/2020GB006769 e2020GB006769.

Higgins, S.R., Jordan, G., Eggleston, C.M., Knauss, K.G., 1998. Dissolution kinetics of the barium sulfate (001) surface by hydrothermal atomic force microscopy. Langmuir 14, 4967–4971. https://doi.org/10.1021/la9806606.

Horner, T.J., Crockford, P.W., 2021. Barium Isotopes: Drivers, Dependencies, and Distributions Through Space and Time. Cambridge University Press. https://doi.org/ 10.1017/7981108865845.

Horner, T.J., Kinsley, C.W., Nielsen, S.G., 2015. Barium-isotopic fractionation in seawater mediated by barite cycling and oceanic circulation. Earth Planet. Sci. Lett. 430, 511–522. https://doi.org/10.1016/j.epsl.2015.07.027.

Hsieh, Y.T., Henderson, G.M., 2017. Barium stable isotopes in the global ocean: tracer of Ba inputs and utilization. Earth Planet. Sci. Lett. 473, 269–278. https://doi.org/ 10.1016/j.epsl.2017.06.024.

Iversen, M.H., Ploug, H., 2010. Ballast minerals and the sinking carbon flux in the ocean: carbon-specific respiration rates and sinking velocity of marine snow aggregates. Biogeosciences 7, 2613–2624. https://doi.org/10.5194/bg-7-2613-2010.

Judat, B., Kind, M., 2004. Morphology and internal structure of barium sulfate—derivation of a new growth mechanism. J. Colloid Interface Sci. 269, 341–353. https://doi.org/10.1016/j.jcis.2003.07.047.

Kamal, M.S., Hussein, I., Mahmoud, M., Sultan, A.S., Saad, M.A., 2018. Oilfield scale formation and chemical removal: a review. J. Pet. Sci. Eng. 171, 127–139. https://doi.org/10.1016/j.petrol.2018.07.037.

Kügler, R.T., Doyle, S., Kind, M., 2015. Fundamental insights into barium sulfate precipitation by time-resolved in situ synchrotron radiation wide-angle X-ray scattering (WAXS). Chem. Eng. Sci. 133, 140–147. https://doi.org/10.1016/j.ces.2014.12.024.

Lam, P.J., Doney, S.C., Bishop, J.K.B., 2011. The dynamic ocean biological pump: Insights from a global compilation of particulate organic carbon, $CaCO_3$, and opal concentration profiles from the mesopelagic. Glob. Biogeochem. Cycles 25, GB3009. https://doi.org/10.1029/2010GB003868.

Laurenceau-Cornec, E.C., Le Moigne, F.A.C., Gallinari, M., Moriceau, B., Toullec, J., Iversen, M.H., Engel, A., De La Rocha, C.L., 2020. New guidelines for the application of Stokes' models to the sinking velocity of marine aggregates. Limnol. Oceanogr. 65, 1264–1285. https://doi.org/10.1002/lno.11388.

Light, T., Norris, R., 2021. Quantitative visual analysis of marine barite microcrystals: insights into precipitation and dissolution dynamics. Limnol. Oceanogr. 66, 3619–3629. https://doi.org/10.1002/lno.11902.

Lopes, C., Kucera, M., Mix, A.C., 2015. Climate change decouples oceanic primary and export productivity and organic carbon burial. Proc. Natl. Acad. Sci. 112, 332–335. https://doi.org/10.1073/pnas.1410480111.

Loubere, P., 1991. Deep-sea benthic foraminiferal assemblage response to a surface ocean productivity gradient: a test. Paleocenography 6, 193–204. https://doi.org/10.1029/90PA02612.

Lüttge, A., 2005. Etch pit coalescence, surface area, and overall mineral dissolution rates. Am. Mineral. 90, 1776–1783. https://doi.org/10.2138/am.2005.1734.

Ma, Z., Ravelo, A.C., Liu, Z., Zhou, L., Paytan, A., 2015. Export production fluctuations in the eastern equatorial Pacific during the Pliocene-Pleistocene: reconstruction using barite accumulation rates. Paleoceanography 30, 1455–1469. https://doi.org/10.1002/2015PA002860.

Marchisio, D.L., Barresi, A.A., Garbero, M., 2002. Nucleation, growth, and agglomeration in barium sulfate turbulent precipitation. AICHE J. 48, 2039–2050. https://doi.org/10.1002/aic.690480917.

Martinez-Ruiz, F., Jroundi, F., Paytan, A., Guerra-Tschuschke, I., del Abad, M.M., González-Muñoz, M.T., 2018. Barium bioaccumulation by bacterial biofilms and implications for Ba cycling and use of Ba proxies. Nat. Commun. 9, 1619. https://doi.org/10.1038/s41467-018-04069-z.

Martinez-Ruiz, F., Paytan, A., Gonzalez-Muñoz, M.T., Jroundi, F., Abad, M.D.M., Lam, P.J., Bishop, J.K.B., Horner, T.J., Morton, P.L., Kastner, M., 2019. Barite formation in the ocean: Origin of amorphous and crystalline precipitates. Chem. Geol. 511, 441–451. https://doi.org/10.1016/j.chemgeo.2018.09.011.

Martinez-Ruiz, F., Paytan, A., Gonzalez-Muñoz, M.T., Jroundi, F., Abad, M.D.M., Lam, P.J., Horner, T.J., Kastner, M., 2020. Barite precipitation on suspended organic matter in the mesopelagic zone. Front. Earth Sci. 8, 567714. https://doi.org/10.3389/feart.2020.567714.

McNown, J., Malaika, J., 1950. Effects of particle shape on settling velocity at low Reynolds numbers. Trans. Am. Geophys. Union 31, 74–82. https://doi.org/10.1029/TR031i001p00074.

Mete, Ö., Subhas, A., Kim, H., Dunlea, A., Whitmore, L., Shiller, A., Gilbert, M., Leavitt, W., Horner, T., 2023. Barium in seawater: dissolved distribution, relationship to silicon, and barite saturation state determined using machine learning. Earth Syst. Sci. Data Discuss. 1–42. https://doi.org/10.5194/essd-2023-67.

Middleton, J.T., Hong, W.L., Paytan, A., Auro, M.E., Griffith, E.M., Horner, T.J., 2023. Barium isotope fractionation in barite–fluid systems at chemical equilibrium. Chem. Geol. 121453. https://doi.org/10.1016/j.chemgeo.2023.121453.

Monnin, C., Cividini, D., 2006. The saturation state of the world's ocean with respect to (Ba, Sr) $SO_4$ solid solutions. Geochim. Cosmoshim. Acta 70, 3290–3298. https://doi.org/10.1016/j.gca.2006.04.002.

Monnin, C., Jeandel, C., Cattaldo, T., Dehairs, F., 1999. The marine barite saturation state of the world's oceans. Mar. Chem. 65, 253–261. https://doi.org/10.1016/S0304-4203(99)00016-X.

Moore Jr., T.C., Wade, B.S., Westerhold, T., Erhardt, A.M., Coxall, H.K., Baldauf, J., Wagner, M., 2014. Equatorial Pacific productivity changes near the Eocene-Oligocene boundary. Paleoceanography 29, 825–844. https://doi.org/10.1002/2014PA002656.

Nancollas, G.H., Liu, S.T., 1975. Crystal growth and dissolution of barium sulfate. Soc. Pet. Eng. J. 15, 509–516. https://doi.org/10.2118/5300-PA.

Nayar, K.G., Sharqawy, M.H., Banchik, L.D., Lienhard, V.J.H., 2016. Thermophysical properties of seawater: a review and new correlations that include pressure dependence. Desalination 390, 1–24. https://doi.org/10.1016/j.desal.2016.02.024.

Nowicki, M., DeVries, T., Siegel, D.A., 2022. Quantifying the carbon export and sequestration pathways of the ocean's biological carbon pump. Glob. Biogeochem. Cycles 36. https://doi.org/10.1029/2021GB007083 e2021GB007083.

Nürnberg, C.C., Bohrmann, G., Schlüter, M., Frank, M., 1997. Barium accumulation in the Atlantic sector of the Southern Ocean: results from 190,000-year records. Paleoceanography 12, 594–603. https://doi.org/10.1029/97PA01130.

Ouyang, B., Akob, D.M., Dunlap, D., Renock, D., 2017. Microbially mediated barite dissolution in anoxic brines. Appl. Geochem. 76, 51–59. https://doi.org/10.1016/j.apgeochem.2016.11.008.

Ouyang, B., Renock, D., Akob, D.M., 2019. Effects of organic ligands and background electrolytes on barite dissolution. Geochim. Cosmochim. Acta 256, 6–19. https://doi.org/10.1016/j.gca.2018.02.003.

Paytan, A., Griffith, E.M., 2007. Marine barite: recorder of variations in ocean export productivity. Deep Sea Res. Part II: Top. Stud. Oceanogr. 54, 687–705. https://doi.org/10.1016/j.dsr2.2007.01.007.

Paytan, A., Kastner, M., 1996. Benthic Ba fluxes in the central Equatorial Pacific, implications for the oceanic Ba cycle. Earth Planet. Sci. Lett. 142, 439–450. https://doi.org/10.1016/0012-821X(96)00120-3.

Paytan, A., Kastner, M., Chavez, F.P., 1996. Glacial to interglacial fluctuations in productivity in the equatorial pacific as indicated by marine barite. Science 274, 1355–1357. https://doi.org/10.1126/science.274.5291.1355.

Paytan, A., Averyt, K., Faul, K., Gray, E., Thomas, E., 2007. Barite accumulation, ocean productivity, and Sr/Ba in barite across the Paleocene–Eocene thermal maximum. Geology 35, 1139–1142. https://doi.org/10.1130/G24162A.1.

Pedersen, T.F., Calvert, S.E., 1990. Anoxia vs. productivity: what controls the formation of organic-carbon-rich sediments and sedimentary rocks? AAPG Bull. 74, 454–466. https://doi.org/10.1306/0C9B232B-1710-11D7-8645000102C1865D.

Ploug, H., 2001. Small-scale oxygen fluxes and remineralization in sinking aggregates. Limnol. Oceanogr. 46, 1624–1631. https://doi.org/10.4319/lo.2001.46.7.1624.

Ploug, H., Hietanen, S., Kuparinen, J., 2002. Diffusion and advection within and around sinking, porous diatom aggregates. Limnol. Oceanogr. 47, 1129–1136. https://doi.org/10.4319/lo.2002.47.4.1129.

Prairie, J.C., Montgomery, Q.W., Proctor, K.W., Ghiorso, K.S., 2019. Effects of phytoplankton growth phase on settling properties of marine aggregates. J. Mar. Sci. Eng. 7, 265. https://doi.org/10.3390/jmse7080265.

R Core Team, 2020. R: A Language and Environment for Statistical Computing. R Foundation for Statistical Computing, Vienna, Austria.

Ragueneau, O., Tréguer, P., Leynaert, A., Anderson, R.F., Brzezinski, M.A., DeMaster, D.J., Dugdale, R.C., Dymond, J., Fischer, G., François, R., Heinze, C., 2000. A review of the Si cycle in the modern ocean: recent progress and missing gaps in the application of biogenic opal as a paleoproductivity proxy. Glob. Planet. Chang. 26, 317–365. https://doi.org/10.1016/S0921-8181(00)00052-7.

Rahman, S., Shiller, A.M., Anderson, R.F., Charette, M.A., Hayes, C.T., Gilbert, M., Grissom, K.R., Lam, P.J., Ohnemus, D.C., Pavia, F.J., Twining, B.S., Vivancos, S.M., 2022. Dissolved and particulate barium distributions along the US GEOTRACES North Atlantic and East Pacific Zonal Transects (GA03 and GP16): global implications for the marine barium cycle. Glob. Biogeochem. Cycles 36. https://doi.org/10.1029/2022GB007330 e2022GB007330.

Reolid, M., Martínez-Ruiz, F., 2012. Comparison of benthic foraminifera and geochemical proxies in shelf deposits from the Upper Jurassic of the Prebetic (southern Spain). J. Iber. Geol. 38, 449–465. https://doi.org/10.5209/rev_JIGE.2012.v38.n2.40468.

Robin, E., Rabouille, C., Martinez, G., Lefevre, I., Reyss, J.L., Van Beek, P., Jeandel, C., 2003. Direct barite determination using SEM/EDS-ACC system: implication for constraining barium carriers and barite preservation in marine sediments. Mar. Chem. 82, 289–306. https://doi.org/10.1016/S0304-4203(03)00075-6.

Rushdi, A.I., McManus, J., Collier, R.W., 2000. Marine barite and celestite saturation in seawater. Mar. Chem. 69, 19–31. https://doi.org/10.1016/S0304-4203(99)00089-4.

Sanders, R., Henson, S.A., Koski, M., De La Rocha, C.L., Painter, S.C., Poulton, A.J., Riley, J., Salihoglu, B., Visser, A., Yool, A., Bellerby, R., Martin, A.P., 2014. The biological carbon pump in the North Atlantic. Prog. Oceanogr. 129, 200–218. https://doi.org/10.1016/j.pocean.2014.05.005.

Schenau, S.J., De Lange, G.J., 2001. Phosphorus regeneration vs. burial in sediments of the Arabian Sea. Mar. Chem. 75, 201–217. https://doi.org/10.1016/S0304-4203(01)00037-8.

Schindelin, J., Arganda-Carreras, I., Frise, E., Kaynig, V., Longair, M., Pietzsch, T., Preibisch, S., Rueden, C., Saalfeld, S., Schmid, B., Tinevez, J.-Y., White, D.J., Hartenstein, V., Eliceiri, K., Tomancak, P., Cardona, A., 2012. Fiji: an open-source platform for biological-image analysis. Nat. Methods 9, 676–682. https://doi.org/10.1038/nmeth.2019.

Schindelin, J., Rueden, C.T., Hiner, M.C., Eliceiri, K.W., 2015. The ImageJ ecosystem: an open platform for biomedical image analysis. Mol. Reprod. Dev. 82, 518–529. https://doi.org/10.1002/mrd.22489.

Schoepfer, S.D., Shen, J., Wei, H., Tyson, R.V., Ingall, E., Algeo, T.J., 2015. Total organic carbon, organic phosphorus, and biogenic barium fluxes as proxies for paleomarine productivity. Earth-Sci. Rev. Part II 149, 23–52. https://doi.org/10.1016/j.earscirev.2014.08.017.

Serno, S., Winckler, G., Anderson, R.F., Hayes, C.T., Ren, H., Gersonde, R., Haug, G.H., 2014. Using the natural spatial pattern of marine productivity in the Subarctic North Pacific to evaluate paleoproductivity proxies. Paleoceanography 29, 438–453. https://doi.org/10.1002/2013PA002594.

Sharqawy, M.H., Lienhard, J.H., Zubair, S.M., 2010. Thermophysical properties of seawater: a review of existing correlations and data. Desalin. Water Treat. 16, 354–380. https://doi.org/10.5004/dwt.2010.1079.

Shen, W., Qiao, S., Sun, R., He, Z., Wu, B., Jin, L., Chen, L., Yin, Z., Ge, C., Shi, X., Sheng, J., 2023. Distribution pattern of planktonic and benthic foraminifera in surface sediments near the equatorial western Indian Ocean and its indications of paleo-environment and productivity. J. Asian Earth Sci. 250, 105635. https://doi.org/10.1016/j.jseaes.2023.105635.

Simon, M., Grossart, H., Schweitzer, B., Ploug, H., 2002. Microbial ecology of organic aggregates in aquatic ecosystems. Aquat. Microb. Ecol. 28, 175–211. https://doi.org/10.3354/ame028175.

Sun, X., Yang, Z., Fan, D., Li, Y., 2015. Crystals of suspended marine barite in the eastern equatorial Pacific: processes of dissolution and effects on crystal morphology. Chin. J. Oceanol. Limnol. 33, 194–203. https://doi.org/10.1007/s00343-015-3353-1.

Torfstein, A., Winckler, G., Tripati, A., 2010. Productivity feedback did not terminate the Paleocene-Eocene thermal maximum (PETM). Clim. Past 6, 265–272. https://doi.org/10.5194/cp-6-265-2010.

Torres-Crespo, N., Martínez-Ruiz, F., González-Muñoz, M.T., Bedmar, E.J., De Lange, G.J., Jroundi, F., 2015. Role of bacteria in marine barite precipitation: a case study

using Mediterranean seawater. Sci. Total Environ. 512, 562–571. https://doi.org/10.1016/j.scitotenv.2015.01.044.

Trindade Pedrosa, E., Kurganskaya, I., Fischer, C., Luttge, A., 2019. A statistical approach for analysis of dissolution rates including surface morphology. Minerals 9, 458. https://doi.org/10.3390/min9080458.

Van Beek, P., Reyss, J.L., Bonte, P., Schmidt, S., 2003. Sr/Ba in barite: a proxy of barite preservation in marine sediments? Mar. Geol. 199, 205–220. https://doi.org/10.1016/S0025-3227(03)00220-2.

van der Jagt, H., Friese, C., Stuut, J.-B.W., Fischer, G., Iversen, M.H., 2018. The ballasting effect of Saharan dust deposition on aggregate dynamics and carbon export: aggregation, settling, and scavenging potential of marine snow. Limnol. Oceanogr. 63, 1386–1394. https://doi.org/10.1002/lno.10779.

Wickham, H., 2016. ggplot2: Elegant Graphics for Data Analysis. Springer-Verlag, New York.

Widanagamage, I.H., Schauble, E.A., Scher, H.D., Griffith, E.M., 2014. Stable strontium isotope fractionation in synthetic barite. Geochim. Cosmochim. Acta 147, 58–75.

Winckler, G., Anderson, R.F., Jaccard, S.L., Marcantonio, F., 2016. Ocean dynamics, not dust, have controlled equatorial Pacific productivity over the past 500,000 years. Proc. Natl. Acad. Sci. 113, 6119–6124. https://doi.org/10.1073/pnas.1600616113.

Xiao, C., Wang, Y., Tian, J., 2022. Formation of marine barite in the deep-sea environment: evidence from sinking particles in the challenger deep, Mariana Trench. Reg. Stud. Mar. Sci. 50, 102159. https://doi.org/10.1016/j.rsma.2021.102159.

Yao, W., Griffith, E., Paytan, A., 2020. Pelagic Barite: Tracer of Ocean Productivity and a Recorder of Isotopic Compositions of Seawater S, O, Sr, Ca and Ba. Cambridge University Press. https://doi.org/10.1017/9781108847162.

Zetsche, E.M., Larsson, A.I., Iversen, M.H., Ploug, H., 2020. Flow and diffusion around and within diatom aggregates: effects of aggregate composition and shape. Limnol. Oceanogr. 65, 1818–1833. https://doi.org/10.1002/lno.11420.

Zhen-Wu, B.Y., Dideriksen, K., Olsson, J., Raahauge, P.J., Stipp, S.L.S., Oelkers, E.H., 2016. Experimental determination of barite dissolution and precipitation rates as a function of temperature and aqueous fluid composition. Geochim. Cosmochim. Acta 194, 193–210. https://doi.org/10.1016/j.gca.2016.08.041.

Ziervogel, K., Steen, A.D., Arnosti, C., 2010. Changes in the spectrum and rates of extracellular enzyme activities in seawater following aggregate formation. Biogeosciences 7, 1007–1015. https://doi.org/10.5194/bg-7-1007-2010.

Horner, T.J., Little, S.H., Conway, T.M., Farmer, J.R., Hertzberg, J.E., Janssen, D.J., Lough, A.J.M., McKay, J., Tessin, A., Galer, S.J.G., Jaccard, S.L., Lacan, F., Paytan, A., Wuttig, K., Bolton, C., Calvo, E., Cardinal, D., de Garidel-Thoron, T., Fietz, S., Hendry, K., Marcantonio, F., Rafter, P., Ren, H., Somes, C., Sutton, J., Torfstein, A., Winckler, G., 2021. Bioactive trace metals and their isotopes as paleoproductivity proxies: an assessment using GEOTRACES-era data. Glob. Biogeochem. Cycles 35, e2020GB006814. https://doi.org/10.1029/2020GB006814.